PNAS RESEARCH ARTICLE | APPLIED PHYSICAL SCIENCES

Aging of amorphous materials under cyclic strain

Dor Shohat[a,b,1], Paul Baconnier[c,1], Itamar Procaccia[d,e], Martin van Hecke[c,f], and Yoav Lahini[a,b,2]

Affiliations are included on p. 10.

Edited by Ludovic Berthier, Universite de Montpellier, Montpellier, France; received June 11, 2025; accepted November 22, 2025 by Editorial Board Member Daan Frenkel

Amorphous materials driven away from equilibrium display a diverse repertoire of complex, history-dependent behaviors. One striking feature is a failure to return to equilibrium after an abrupt change in otherwise static external conditions. Instead, amorphous materials often exhibit physical aging: an ever-slowing, nonexponential relaxation that can span a huge range of timescales. Here, we examine the aging behavior of three different amorphous materials subjected to slow periodic driving. The results reveal a generic aging phenomenon characterized by a logarithmic decay of dissipation per cycle. This observation is evaluated against several mesoscopic models of amorphous matter that successfully capture aging under static conditions: i) a collection of noninteracting relaxation processes ii) a noisy hysteron model with random pairwise interactions, and iii) a structural model consisting of a random network of bistable elastic bonds. We find that only the latter model reproduces all experimental findings and relates its success to its persistent, slow exploration of a complex energy landscape with clear signatures of replica symmetry breaking. Thus, cyclic driving emerges as a simple yet powerful protocol to characterize amorphous materials, probe their complex energy landscapes, and distinguish between different models.

aging | amorphous materials | cyclic driving | hysterons

Significance

Understanding how amorphous materials evolve under external driving is essential for predicting their long-term stability and functional performance. This study reveals a universal aging behavior in amorphous materials subjected to cyclic deformation, in the form of a logarithmic decay of energy dissipation per cycle. This finding challenges existing models of amorphous materials and highlights the power of global measurements to probe the complex energy landscapes and self-organization dynamics of these systems. Furthermore, we identify hysteretic aging responses that define a material-specific property. Our results provide a unique perspective on disordered solids, with implications for memory formation, material design, mechanical fatigue, and the broader understanding of out-of-equilibrium systems.

When driven away from equilibrium, amorphous materials exhibit a range of complex, history-dependent responses, such as critical intermittent dynamics (1), anomalously slow relaxations, physical aging (2), and a variety of memory effects (3). This diversity of different behaviors, exhibiting complexity over a wide range of spatial and temporal scales, seems to defy a common description.

The out-of-equilibrium response of amorphous materials to external driving is traditionally studied using two distinct driving protocols (4). The first protocol explores the long-time response to an abrupt stepwise perturbation. Amorphous materials as diverse as glasses and polymers (2, 5), granular packings (6), interfaces (7, 8), and crumpled materials (9, 10) then fail to regain equilibrium and instead exhibit an ever-slowing relaxation process known as "physical aging," in which the system's properties depend on the time elapsed since the perturbation. Theoretically, this phenomenon is usually described as a sluggish, noise-driven exploration of a complex or hierarchical energy landscape (9, 11–14).

The second protocol considers the intermediate time response of amorphous materials to cyclic driving, which has been used to reveal and investigate self-organization (15, 16), memory effects (17–21), emergent computational capabilities (22–24), and yielding (25, 26). As cyclic driving appears to eventually result in a periodic response, these phenomena are usually modeled using athermal quasi-static descriptions (27).

The long term aging behavior during cyclic driving, however, remains underexplored, despite its importance to material properties such as stability (28), yielding, or failure (29–31). Recent works suggest that in the presence of noise, cyclic driving induces a slow evolution of amorphous systems which converge to a limit cycle in the absence of noise (32–35). Simulations revealed that the energy of several model amorphous solids, measured stroboscopically at the end of each driving cycle, exhibits a slow logarithmic decay (35, 36), accompanied by intermittent particle rearrangements (37). Experiments and theory by Bandi et al. on cyclic compression of granular materials observed a power law decay of the energy dissipated per driving cycle (38). These observations are reminiscent of rheological measurements of soft glasses, which often show a slow evolution of the loss modulus at long times (39, 40). Thus, an interesting question is whether these aging behaviors are generic, and what new light can they shed on the physics and modeling of amorphous materials.

Author contributions: D.S., P.B., M.v.H., and Y.L. designed research; D.S., P.B., and I.P. performed research; D.S. and P.B. analyzed data; and D.S., P.B., I.P., M.v.H., and Y.L. wrote the paper.

The authors declare no competing interest.

This article is a PNAS Direct Submission. L.B. is a guest editor invited by the Editorial Board.

[1]D.S. and P.B. contributed equally to this work.

[2]To whom correspondence may be addressed. Email: lahini@tauex.tau.ac.il.

This article contains supporting information online at https://www.pnas.org/lookup/suppl/doi:10.1073/pnas.2515075123/-/DCSupplemental.

Published February 18, 2026.

Here, we describe the results of applying slow cyclic strain to three very different amorphous materials that exhibit aging under fixed strain: crumpled thin sheets, amorphous bundles of metallic fibers, and shape-memory alloys. We have one main experimental finding and one main theoretical realization. Experimentally, we establish the commonality of the response: under cyclic drive these vastly different materials exhibit a remarkably similar aging behavior, characterized by a logarithmic decay in the energy dissipation per cycle. This result, we show, is consistent with the general theoretical framework of ref. 38.

The theoretical realization is that this behavior allows to discern between different mesoscopic models for physical aging. To this end, we confront our experimental results with the predictions of models that capture aging under static conditions. These models adopt a coarse-grained view of amorphous materials, describing them as collections of effective, mesoscopic degrees of freedom. We consider three models with increasing complexity and degree of interactions: i) a noninteracting model assuming independent relaxation processes with a wide Distribution of Relaxation Times (DRT) (10, 41–44); ii) a discrete model which allows for the introduction of random, pairwise interactions (Hysteron model) (45, 46); and iii) a structural model describing amorphous materials as a disordered network of bistable elastic elements (13, 47–49).

We find that only the last model is consistent with all observations, old and new. We show that the decay of the dissipation per cycle is correlated with a decay in the number of bistable elements that switch back and forth during the cycle. We then connect this to the model's slow exploration of its complex energy landscape, where we demonstrate a dynamical signature of replica symmetry breaking (50–54). This key factor is absent in the other models, and we discuss the ingredients that seem to give rise to it. Thus, the long time response of aging materials to cyclic driving offers a characterization of amorphous materials and allows to distinguish between models.

Experiments. We explore three samples of widely different amorphous materials: a thin Mylar sheet crumpled into a ball, an amorphous bundle of metallic fibers (steel wool), and a thin wire of polycrystalline shape-memory alloy (Nitinol in the martensite phase)–see *Insets* in Fig. 1 *A*. The crumpled sheet and steel wool are tested using a custom linear compression stage, while the Nitinol wire is tested using a torsional test device (*Materials and Methods*). Each system is controlled by the imposed displacement U (angle θ for the Nitinol wire), and we measure the time-dependent force $F(t)$ (torque $\Gamma(t)$) exerted by the system in response.

To probe the long-time relaxation after a stepwise perturbation, the displacement (angle) is quenched abruptly to a finite value, and the time-dependent force (torque) is measured. All three systems show logarithmic stress relaxation; the force relaxes logarithmically in time for the crumpled sheet (Fig. 1 *A*, *Top* and refs. 10 and 13), for steel wool (Fig. 1 *A*, *Middle*), and for the Nitinol wire under torsion (Fig. 1 *A*, *Bottom* and *SI Appendix*).

Next we consider cyclic driving, where the displacement (angle) oscillates along the interval $[U_{\min}, U_{\max}]$ ($[\theta_{\min}, \theta_{\max}]$), for $n \leq 3{,}000$ cycles* (Fig. 1*B*). The three resulting response curves corresponding to the three different materials, $F(U)$ and $\Gamma(\theta)$, show similar dynamics in the form of hysteresis loops with two distinct characteristics.

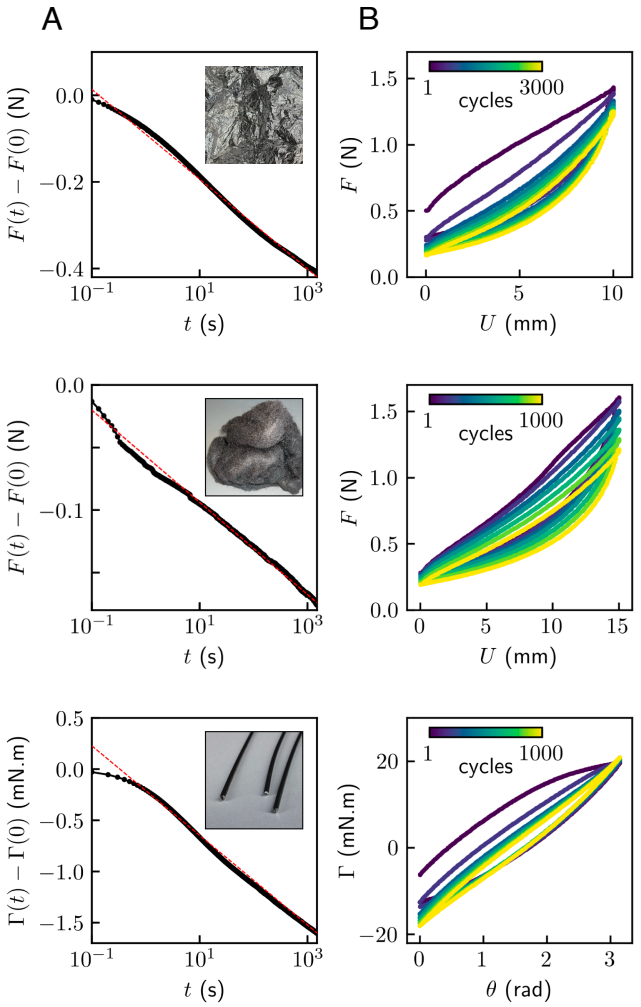

Fig. 1. Static and cyclic drive experiments with different amorphous materials. From *Top* to *Bottom*: crumpled sheet, steel wool, and Nitinol wire in torsion. (*A*) Force (torque) relaxation at fixed displacement U (angle θ); the red dashed line represents logarithmic evolution; *Inset*: snapshots of the different experimental systems. (*B*) Force–displacement curves for repeated cyclic drive, color coded from blue to yellow as time increases; only a few cycles n are shown for clarity: $n = 1, 3, 10, 30, 100, 300, 1{,}000$.

First, the force at a given displacement along the n-th cycle $F_n(U)$ (or torque at a given angle $\Gamma_n(\theta)$) asymptotically scales as $F_n(U) \sim C(U) \log n$, where $C(U)$ is a prefactor that depends both on the displacement and the drive direction (Fig. 2*A*). This holds for any strain along the driving cycle, in both the ascending and descending branches (*SI Appendix*). The overall response is fully characterized by the function $C(U)$, which we dub the Material Creep Function, which describes the hysteretic, displacement-dependent logarithmic prefactor of $F_n(U)$ (Fig. 2 *C–E*). Its shape varies between different amorphous materials, and thus may be used to characterize them. Nevertheless, its hysteretic shape demonstrates a general property of cyclic aging—the force relaxation at each strain is history dependent and is always faster in the ascending branch.

Second, the area enclosed by the hysteresis loop, indicating the dissipated energy per cycle, decays initially as a power law and eventually logarithmically (Fig. 2*B*). While the crossover between these two regimes appears to be material and protocol dependent, the long-time slow relaxation appears to be universal. It is this behavior that we will show to be sensitive to model details, and hence it is central in distinguishing between different models.

*A cyclic drive experiment with 1,000 cycles lasts approximately one day, limiting the number of decades that can be measured in a reasonable time. In static aging experiments, the same period corresponds to 5 to 6 decades of aging (13).

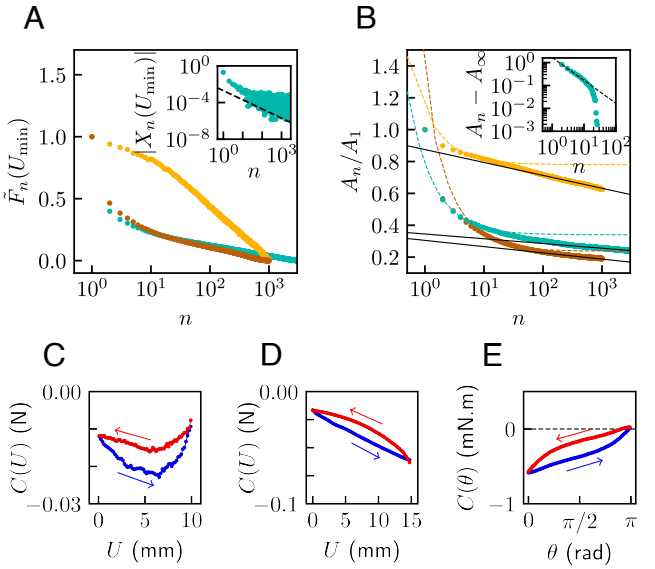

Fig. 2. Experimental characterization of cyclic aging. (*A* and *B*) Different colors correspond to different systems, green: crumpled sheet, orange: steel wool, brown: Nitinol wire. (*A*) Rescaled force $\tilde{F}_n(U) = (F_n(U) - F_{\text{last}}(U)) / (F_0(U) - F_{\text{last}}(U))$ (torque $\tilde{\Gamma}_n(\theta)$ for the Nitinol wire) at the minimum displacement $U_{\min}$ (angle $\theta_{\min}$) as a function of the number of drive cycles n; (*Inset*) Force increment at the minimum displacement $X_n(U_{\min}) = F_{n+1}(U_{\min}) - F_n(U_{\min})$ as a function of the number of drive cycles n for the crumpled sheet. The black dashed line represents $1/n$. (*B*) Dissipation per cycle $A_n = \oint F_n(U)dU$ as a function of n; the solid black lines represent $A_0 + \tilde{C}\log n$, where $\tilde{C}$ is obtained from the loop integral of (*C*–*E*), and the dashed lines represent $A_\infty + a/n$, as obtained from a least square fit; (*Inset*) $A_n - A_\infty$ as a function of the number of drive cycles n for the crumpled sheet; the black dashed lines represent $A_\infty + a/n$. (*C*–*E*) Material creep functions $C(U)$ ($C(\theta)$); blue: ascending, red: descending; *C*: crumpled sheet; *D*: steel wool; and *E*: Nitinol wire.

Theoretical Argument. In previous work, Bandi et al. (38) proposed a general argument for the evolution of the dissipation per cycle A_n for frictional disk packings under cyclic loading (namely force control). The essence of the argument is the existence of an analytic expansion near a fixed point at large n, with the leading term in the expansion governing the aging. For force control, this leads to a power-law decay of the dissipation per cycle. Here, we adapt this framework to account for strain control protocols and find that it is consistent with our experimental findings.[†]

We consider the force increment at a given displacement in the nth driving cycle, $X_n(U) = F_{n+1}(U) - F_n(U)$. This new variable is history dependent and could be expressed as $X_{n+1} = g(X_n)$, where the function $g(x)$ is unknown at this point. X_n must asymptotically vanish, otherwise the force would strongly diverge. Thus $g(x = 0) = 0$, and near this fixed point a *generic* Taylor expansion reads

$$X_{n+1} = g(X_n) = X_n - KX_n^2 + \cdots \qquad [1]$$

Without an (exceptional) symmetry reason, $K \neq 0$. Therefore, asymptotically, we find the scalings $X_n \sim n^{-1}$ and $F_n(U) \sim C(U)\log n$, where $C(U)$ is the material creep function (see *SI Appendix* for derivation and leading correction). The dissipation can be obtained by integrating over the response $A_n = \oint F_n(U)dU \sim \tilde{C}\log n$, where $\tilde{C} = \oint C(U)dU$, resulting in a logarithmic decay that is consistent with our experimental findings (Fig. 2). One should note that in exceptional cases where $K = 0$, higher-order terms will lead to different scaling laws.

In contrast to our cyclic strain protocol, the cyclic loading considered by Bandi et al. (38) defined X_n as the packing fraction increment over driving cycles. This resulted in a different asymptotic scaling of $A_n \sim X_n \sim 1/n$, underscoring that aging under cyclic driving can be protocol-sensitive.

This reasoning, which is consistent with the observed aging under cyclic driving, is based on a simple and general phenomenological argument, hinting at the generality of our observations. Yet, this description does not provide a microscopic understanding of the mechanisms leading to cyclic aging.

Searching for a Minimal Model

To better understand our experimental observations of aging under cyclic drive, we consider three different models that are known to reproduce aging under static drive, and examine their predictions under cyclic driving. These models all adopt a coarse-grained view of amorphous materials, describing them as collections of effective, mesoscopic degrees of freedom. However, the models differ in the choice of these degrees of freedom, and the degree of complexity of their interactions.

Model (i): Distribution of Relaxation Times. Consider first a model of noninteracting degrees of freedom, where slow relaxation under fixed condition is described as the sum response of many exponential relaxations with a wide Distribution of Relaxation Times (DRT). This approach, first used to model the Kohlrausch stretched exponential relaxation (41, 42), was recently shown to account for various aging effects in static and stepwise driving protocols (10, 43, 44). Below, we show that this description fails to capture the experimentally observed aging during cyclic driving.

Following (10), the DRT model is constructed as follows. We assume a system which is controlled by a single parameter U and which evolves via an ensemble of noninteracting exponential relaxation processes, V_λ, each characterized by a relaxation rate λ, where the ensemble has a broad distribution of rates $P(\lambda) \propto 1/\lambda$. A key assumption is that for every U there exists an equilibrium state $V^{eq}(U)$ and that all relaxation modes contribute to it equally, i.e. $V^{eq} = \int_{\lambda_{\min}}^{\lambda_{\max}} P(\lambda)V_\lambda^{eq}$, and $V_\lambda^{eq} = V^{eq}$.

Under static conditions, it was shown in previous work that this DRT model exhibits logarithmic relaxation (43, 44). Namely, from an equilibrium state V_1^{eq}, following an abrupt change in U, its relaxation toward a new equilibrium V_2^{eq} is logarithmic in time as long as the observation time is between the physical cutoffs, $1/\lambda_{\min}$ and $1/\lambda_{\max}$. In subsequent work, the same model was shown to capture the nonmonotonic slow response to a two-step driving protocol, leading to slow, Kovacs-like memory responses (10).

We now extend the model to consider cyclic driving, by oscillating the control parameter U across a dimensionless interval $U \in [0, 1]$, at constant speed $v = |dU/dt|$ (Fig. 3*A*). Each value of U is assigned a different equilibrium state $V^{eq}(U)$, and the relaxation timescales λ are distributed in $\left[10^0, 10^6\right]$ (*SI Appendix*). The system is initiated at equilibrium at $U = 0$. Simulations show that the response at a given U along the cycle, $V_n(U)$, evolves logarithmically (Fig. 3*B*). However, the dissipation per cycle, $A_n = \oint V_n(U,t)dU$, decreases as a power-law with the number of drive cycles n, such that $A_n \propto 1/n$. (Fig. 3*C*).

[†]We adopt the notation of force and displacement, yet the derivation applies to our torsional measurements as well.

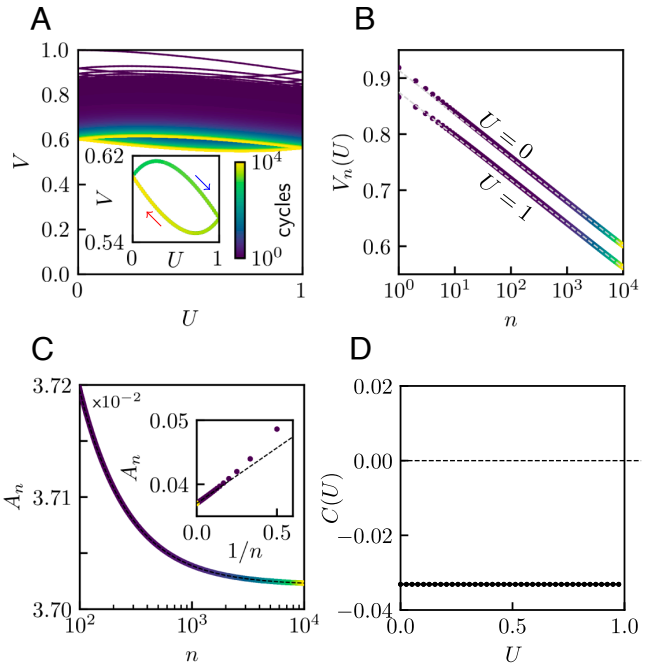

Fig. 3. Cyclic aging in simulations of a DRT model. (*A–C*) Response to a cyclic drive with fixed $V^{eq}(U) = 1 - U$ and $v = 0.2$. (*A*) $V(U, t)$; *Inset*: response to the 4 last cycles. (*B*) $V_n(U)$ as a function of n for the minimum ($U = 0$) and maximum ($U = 1$) sweep; the light gray dashed lines represent the large-n logarithmic evolution, as obtained from a least-square method fit. (*C*) A_n as a function of n; the dashed black line represents $A_\infty + \tilde{D}/n$, as obtained from a least square method fit; *Inset*: as a function of $1/n$. (*D*) Material creep function $C(U)$, evaluated from least-square method fits in $n = [9 \times 10^3, 10^4]$. Note that here, $C(U)$ is constant over the driving range, and does not differ between the ascending and descending branches.

To understand the origin of this power-law decay, we plot the material creep function $C(U)$ as defined above (Fig. 3*D*). We find that $C(U)$ asymptotically forms a straight line, such that the dissipation does not evolve logarithmically. Measuring $C(U)$ after a finite amount of cycles results in a vanishing deviation from the straight line, an artifact originating from the power law convergence of A_n (*SI Appendix*). Thus, the hysteresis loops $V_n(U)$ drift in a logarithmic fashion, while the dissipation per cycle converges to an asymptotic value. In *SI Appendix*, we derive the $A_n \propto 1/n$ scaling analytically for the DRT model under sinusoidal driving as long as the observation time is within the physical cutoffs.

Altogether, this model is not able to reproduce our experimental observations of a hysteretic $C(U)$ and long time logarithmic decay of dissipation under cyclic driving.

Model (ii): Coupled Hysterons. The DRT model does not consider interactions between different relaxation modes. These, however, are expected to play a key role in the aging dynamics (13). To incorporate interactions, we begin by discretizing the model. A discrete version of the DRT model can be constructed by considering N binary and independent relaxation processes, each characterized by a single activation barrier. The distribution of these barriers is taken to be wide, so that at finite temperature, their Arrhenius activation rates are distributed as $P(\lambda) \sim 1/\lambda$ (44). Such model, still without interactions, was shown to reproduce logarithmic aging in static conditions, while partially capturing the temporal statistics of the intermittencies detected in experiments (55).

To consider cyclic driving, we allow the discrete elements to hysterically transition back and forth between their two stable states (49, 56). In the simplest case, such elements can be modeled as "hysterons" (22, 45, 46). Collections of hysterons are often used to account for complex memory effects in amorphous matter under cyclic drive in the a-thermal quasi-static limit (20, 57). In the following, we consider a collection of noisy hysterons (i.e., at a finite temperature), whose individual parameters are chosen to produce stochastic transition rates that are distributed as discussed above. In addition, we consider the effect of introducing pairwise interactions between the hysterons.

We investigate the collective dynamics under static and cyclic drive of ensembles of N hysterons under an external field U (Fig. 4 *A*, *Inset*). Each hysteron i is characterized by a state $s_i = \pm 1$ and two flipping thresholds $U_i^- < U_i^+$, corresponding to the transitions $s_i : -1 \to 1$ and $s_i : 1 \to -1$ respectively. For $U_i^- < U < U_i^+$ the state is determined by the last threshold crossed. The system is characterized by the state $\boldsymbol{s} = (s_1, \ldots, s_N)$, or by its magnetization $m(t) = \sum_i s_i(t)/N$. In the presence of noise and pairwise interactions, the flipping thresholds can be written as

$$U_i^{\pm}(\boldsymbol{s}, t) = u_{i,0}^{\pm} - \sum_{j \neq i} c_{ij} s_j(t) + \sqrt{2T}\xi_i(t), \qquad [2]$$

where $u_{i,0}^{\pm}$ are constants termed the "bare" switching fields, c_{ij} are the interaction coefficients, T is an effective temperature, and the ξ_i are Gaussian white noises with correlations $\langle \xi_i(t)\xi_j(t')\rangle = \delta_{ij}\delta(t - t')$. We take the bare thresholds in a compact range and we flatly sample the interaction coefficients c_{ij} from $[-J_0, J_0]$ (57–60), where J_0 is the typical interaction strength. We focus on reciprocal interactions for which the interaction matrix is symmetric, i.e. $c_{ij} = c_{ji}$, with zero elements along the diagonal. The noninteracting, $J_0 = 0$ case corresponds to the Preisach limit (45), which, as we show below, behaves similarly as the DRT model in the presence of noise. In contrast, $J_0 \geq 0$ allows to explore disordered systems with a given strength of interactions (57, 61). Starting from a random initial condition at $U = 0$, the system is stabilized at zero temperature by flipping unstable hysterons one by one until a stable state is found (60, 62). The dynamics is then integrated using an event-driven Gillespie-like algorithm. See *Materials and Methods* for more details on the choice of parameters and temperature, and on the simulation algorithm.

We first consider static drive conditions, namely an abrupt change of the field from 0 to $U_0 > 0$ at $t = 0$. In the noninteracting case, one can show that the flat threshold distribution for $U > U_0$ approximately gives the $P(\lambda) \sim 1/\lambda$ flipping rate distribution, and simulations confirm that the magnetization $m(t)$ grows logarithmically in time, at a rate that increases with temperature (*SI Appendix*). Finite interaction strengths J_0 do not change qualitatively this picture (Fig. 4*A*), up to the emergence of avalanches and the broadening of the distribution of avalanche size as J_0 increases, leading to large jumps of magnetization at the level of a single-realization. Eventually, for very large J_0 (at fixed T), logarithmic aging slows down and ultimately vanishes. This can be traced to the growing spread of the switching thresholds of the hysterons over a range $\propto J_0$, so that eventually thermal fluctuations are no longer sufficient to overcome these barriers.

Next, we apply cyclic driving by oscillating the field U between 0 and $U_{\max}$ (*Materials and Methods*). First, we consider the case without noise ($T = 0$). After τ cycles the system

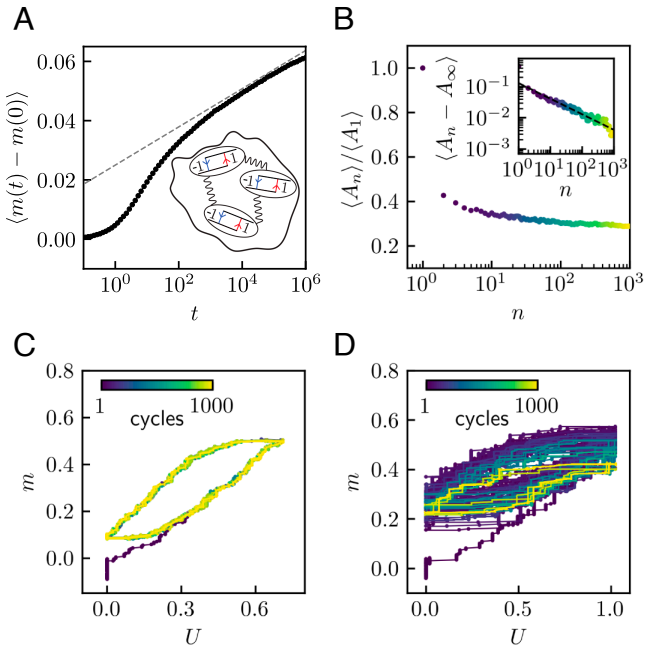

Fig. 4. Interacting hysterons at finite temperature. (*A*) Logarithmic aging under static driving conditions of the ensemble averaged magnetization $\langle m(t) - m(0) \rangle$ as a function of time t (100 samples, $J_0 = 5.10^{-4}$, $N = 2{,}048$, $U_0 = 0.3$, and $T = 10^{-4}$). *Inset*: schematic of interacting hysterons. (*B–D*) Cyclic driving conditions ($v = 1.0$). (*B*) Ensemble averaged, normalized dissipation $\langle A_n \rangle / \langle A_1 \rangle$ as a function of the number of drive cycles n (200 realizations, $N = 2{,}048$, and $T = 10^{-5}$), for large coupling strength $J_0 = 0.15$; data are averaged over cycle number with logarithmically increasing bin sizes. *Inset*: $\langle A_n - A_\infty \rangle$ as a function of n, where A_∞ is obtained by averaging $\langle A_n \rangle$ for $n \in [900, 1{,}000]$; the black dashed line represents the slope 1/2. (*C* and *D*) Magnetization-drive curve $m(U)$ for a single realization for fixed $N = 512$ and $T = 10^{-4}$, for weak ($J_0 = 0.01$, panel *C*) and moderate ($J_0 = 0.077$, panel *D*) interaction strength.

reaches a limit cycle with repeatable sequences of hysteron flips (57, 63, 64). Accordingly, the dissipation per cycle $A_n = \oint m(U) dU$ converges to a fixed value. In the small coupling limit $NJ_0 \ll 1$, $\tau = 1$ for any driving amplitude. In contrast, for $NJ_0 \gg 1$, $\langle \tau \rangle$ is larger than 1, independent of J_0, and depends on $U_{\max}$ without any sign of divergence (*SI Appendix*). Second, we consider a small but finite temperature (*Materials and Methods*), weak interactions ($NJ_0 \ll 1$), and drive the system at a fixed speed $v = |dU/dt|$, ensuring that the drive period remains short compared to the relaxation timescales in the absence of driving (*Materials and Methods*). We find that $\langle A_n \rangle$ decreases abruptly between the first and the second driving cycle, after which the system gets trapped in a limit cycle and fluctuates around it (Fig. 4*C* and *SI Appendix*). Third, for small temperature and moderate to large interactions, thermal fluctuations allow exploration of the space of possible limit cycles, and the response then exhibits abrupt jumps of magnetization due to interaction-induced avalanches (Fig. 4 *B* and *D*). While the relaxation spans multiple drive cycles, our data suggest that the mean dissipation per cycle $\langle A_n \rangle$ decays as a power-law $\langle A_n \rangle \sim 1/n^\alpha$, with $\alpha = 0.5 \pm 0.1$ (Fig. 4 *B* and *D*). Examining the evolution of individual realizations reveals that these eventually hop between a small number of limit cycles and cease to evolve, as we will see below.

Altogether, the thermal coupled-hysterons model captures logarithmic aging in static drive conditions, but seems to fail in reproducing our experimental observation of logarithmic decay of the dissipation under cyclic driving conditions.

Model (iii): Network of Bistable Springs. Finally, we study a structural model composed of a network of bistable elastic bonds (47, 48) (Fig. 5*A*). This model was recently shown to capture both memory effects under cyclic driving at zero temperature (49), and logarithmic aging under static loading at finite temperature (13). In contrast to hysteron models, here the degrees of freedom are continuous. Furthermore, the physical coupling between the bistable elements, along with geometric nonlinearities, leads to complex interactions that can be nonpairwise (65). As we show below, this model successfully captures all of our experimental observations.

Following (13, 49), we consider disordered networks of N_b bonds, where each bond has a double well potential of the form

$$U_i = \frac{\alpha_4}{4} \delta R^4 - \frac{\alpha_2}{2} \delta R^2 \,, \qquad [3]$$

with α_2 and α_4 network constants, and δR_i is the deviation of the i^{th} bond from its randomized rest length $R_i^{(0)}$ (*Materials and Methods*). Due to the inherent incompatibility between bond lengths, the network carries excess stresses and bonds deviate from the minima of their potentials. This leads to an important difference between this and the previous model: while in the hysteron model the wide distribution of activation threshold (and correspondingly, activations time scales) is prescribed by the thresholds of individual hysterons, here this wide distribution emerges from the self-organized collective state of all bistable springs (47).

We simulate the networks using overdamped Langevin dynamics via LAMMPS (66) (*Materials and Methods*). In the simulations, we control the area strain of the network $\gamma(t) = (L^2(t) - L_0^2)/L_0^2$, where L is the system size, while measuring its pressure p. A small temperature T serves as external noise (13).

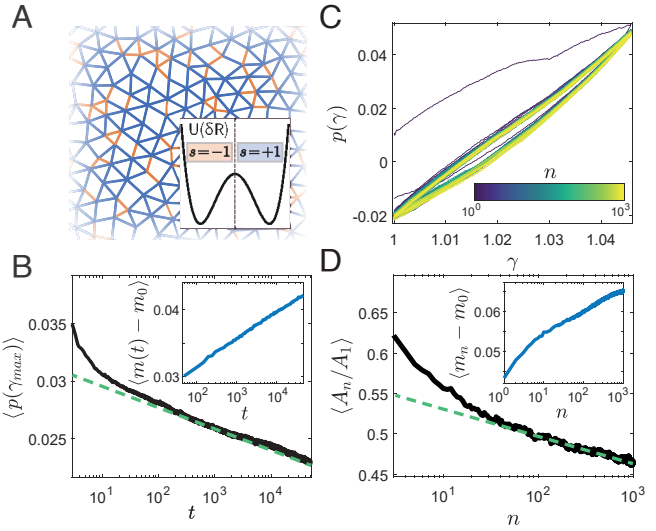

Fig. 5. Simulations of bistable spring networks. (*A*) Illustration of a disordered network with bonds colored by their binary state, red (blue) for $s = -1$ ($s = 1$), and the bistable single bond potential as a function of its displacement δR; (*B*) Static drive conditions: ensemble averaged pressure p as a function of time t for $N = 10^4$ and $T = 0.1$ after a rapid increase of strain γ from 0 to $\gamma_{\max} = 0.045$. The *Inset* shows the change in magnetization over time, which evolves logarithmically as well; (*C*) Mechanical response $p(\gamma)$ under cyclic driving for a single realization with $T = 0.01$; (*D*) Ensemble averaged, normalized dissipation as a function of the driving cycle $\langle A_n / A_1 \rangle$ (same simulation parameters as panel *C*), well captured by a logarithmic evolution at long times (dashed line). The *Inset* shows the change in magnetization over cycles, evaluated stroboscopically at $\gamma = 0$, which evolves logarithmically as well.

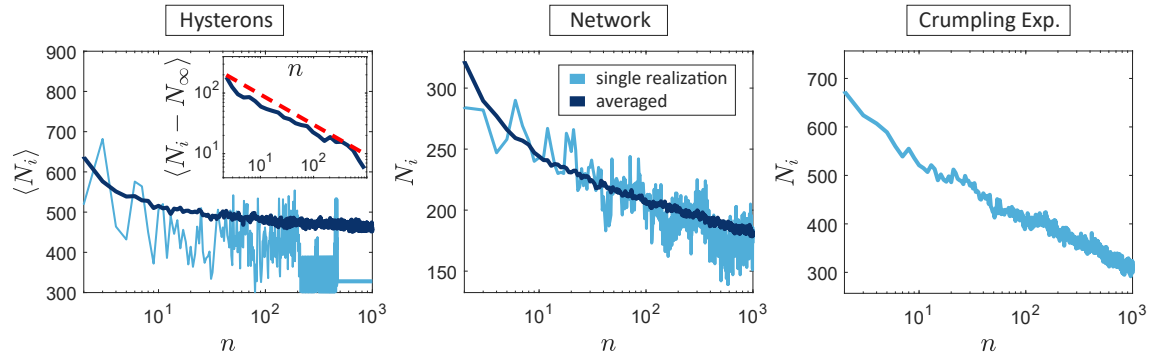

Fig. 6. Structural origin of the decreasing dissipation per cycle. The latter stems from the decreasing number of instabilities along a full driving cycle $N_i(n)$. For the hysteron model (*Left*, $N = 2{,}048$ hysterons, $J_0 = 0.15$, $T = 10^{-5}$, and 200 realizations), $\langle N_i \rangle$ decreases as a power law with the cycle number n; the *Inset* shows a convergence to an asymptotical value N_∞ which scales as $\sim n^{-0.5}$ (dashed red line). The network model (*Middle* panel, $N_b = 5{,}000$ bonds, 50 realizations) exhibits a logarithmic decrease of N_i with the cycle number n, both at the single realization level and on average. In experiments with crumpled sheets (*Right*, single realization) the number of instabilities is measured by counting acoustic emissions during cyclic driving, and exhibits a clear logarithmic decrease.

We set $T \ll \Delta U_0$, where $\Delta U_0 = \alpha_2^2/(4\alpha_4)$ is the energy barrier for an individual bond. We also define the binarized bond state $s_i = \{-1, 1\}$ based on $\mathrm{sgn}(\delta R_i)$, for bonds in their short and long states, respectively. Before applying strain, networks are equilibrated at $T = 0$. See *Materials and Methods* for more details on the choice of parameters and network preparation protocol.

Under constant driving, namely when the strain is suddenly increased to $\gamma = 0.045$, and $T = 0.1$, the pressure exhibits a slow, logarithmic decay (13) (Fig. 5*B*), whose slope increases with temperature (*SI Appendix*). Alternatively, one can observe this slow evolution by tracking the binarized magnetization of the system $m = \sum s_i/N_b$. The change in magnetization $m(t) - m(0)$ exhibits a slow logarithmic evolution similarly to the pressure (*Inset* of Fig. 5*B*).

Next, we subject the networks to biaxial cyclic strain between $\gamma = 0$ and $\gamma = 0.045$. At $T = 0$ the mechanical response $p(\gamma)$ reaches a limit cycle after a few oscillations (49), similarly to the hysteron model. The driving velocity $v = |d\gamma/dt|$ is tuned such that the dissipation $A = \oint p\, d\gamma$ does not strongly depend on v (34) (*SI Appendix*). At finite temperature, however, the dissipation A_n displays a slow, logarithmic evolution over driving cycles n, matching our experimental observations (Fig. 5 *C* and *D*). This slow relaxation is also apparent in the evolution of the magnetization m_n, evaluated stroboscopically at $\gamma = 0$ in each cycle (*Inset* of Fig. 5*D*). In *SI Appendix*, we show the Material Creep Function for this model, which forms a closed loop, and explore the temperature dependence.

Thus, we can capture the aging behavior under cyclic driving with a structural model of coupled instabilities. The emergence of cyclic aging both in the global mechanical properties (pressure and strain) and in the local state of the bistable units, will now allow us to shed light on its origin.

Origin of the Decrease in Dissipation. Equipped with a model that captures our experimental observations, we are now poised to uncover the structural origin underlying the decreasing dissipation over driving cycles (67).

Despite their different behaviors at long times, we find that the decrease of the dissipation per cycle in both the hysteron and network models is associated with a decrease in the number of elements that are activated during a cycle N_i as n increases[‡] (*Materials and Methods*). In the network model, the number of elements involved N_i decreases logarithmically with n, both at the level of a single realization and on average (Fig. 6, *Middle*). For coupled hysterons, at long times, we observe the system hopping between a few discrete values (Fig. 6, *Left*). On average, consistently with the evolution of the dissipation per cycle, N_i seems to decrease as a power law to an asymptotic value (*Inset* of Fig. 6, *Left*). We note that based on the data, we cannot rule out a minute logarithmic decay at very long times. If that is the case, however, this logarithmic decay appears to be much weaker than in the network model.

Next, we test this prediction in experiment, by measuring the acoustic emissions of the crumpled sheet as it ages under cyclic drive. These acoustic emissions have been shown to originate from the activation of snap-trough instabilities in the sheet, the same instabilities that are modeled here as mechanical hysterons or bistable springs (49, 68, 69). Moreover, recent work established that the collective dynamics of these instabilities governs aging under static conditions, without requiring material plasticity (13, 55).

Using these acoustic measurement, we count the number of instabilities at each driving cycle N_i as a function of the cycle number (*Materials and Methods*). The results are presented in Fig. 6, *Right*. These indicate that, as predicted by the network model, the number of instabilities activated in each cycle decays logarithmically with the cycle number. This suggests the interpretation that similarly to the network model, under cyclic drive the crumpled sheet continues to explore its state space, settling into approximate limit cycles with less and less instabilities, and therefore less and less dissipation. We note that here, the number of "clicks" is an underestimation of the true number of instabilities due to the microphone's finite temporal resolution.

Exploring the Configuration Space During Cyclic Aging. The interacting hysteron model and the network model are similar in spirit, introducing interactions between hysteretic two-state degrees of freedom. Nevertheless, while the network model captures all our observations, the hysteron model fails to do so. The network model continues to explore new cycles with reduced dissipation and less participating elements, while the hysteron model eventually remains trapped between a few limit cycles (Fig. 6). In order to pinpoint the reason for this difference, we measure how the two models explore their state space during the slow evolution.

[‡]This is true on average. At the level of a single realization, the number of elements flipping in a cycle N_i is not necessarily monotonic with n. This is evident in Fig. 6.

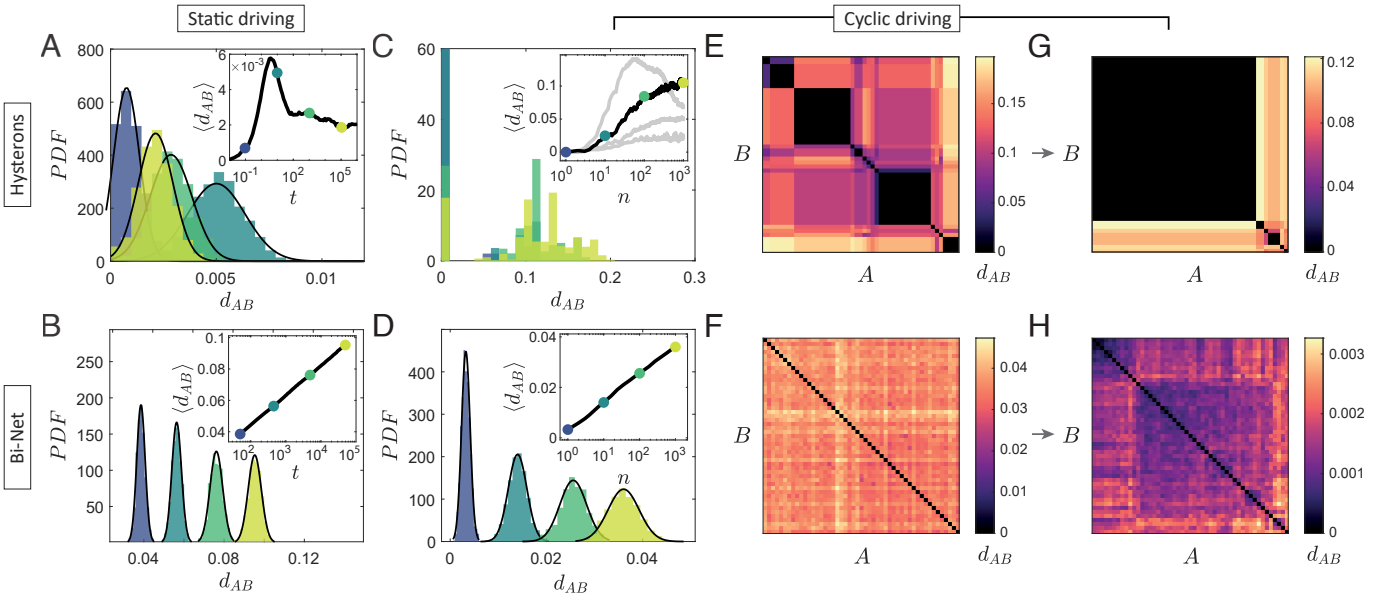

Fig. 7. State space exploration in the different models. Simulation results of coupled hysterons (*Top*), and networks of bistable springs (*Bottom*) in the isoconfigurational ensemble. (*A* and *B*) Distributions of interrealization distances $P(d_{AB})$ at different times under static driving, and the mean distance $\langle d_{AB}(t) \rangle$ (*Inset*). Hysterons converge to a fixed distribution while copies of the bistable network diverge from each other. (*C* and *D*) Distributions of interrealization distances $P(d_{AB})$ at different cycles under cyclic driving, and the mean distance $\langle d_{AB}(n) \rangle$ (*Inset*). Here d_{AB} is evaluated at the beginning of each cycle. We observe a similar scenario where hysterons converge to a discrete number of limit cycles, while bistable networks slowly diverge from each other. For the hysteron model, we also show $\langle d_{AB} \rangle$ for several realizations (gray lines). (*E* and *F*) d_{AB} in a matrix form for the same data, comparing all pairs of realizations at $n = 10^3$, highlights the difference between the models. (*G* and *H*) Results for an isoconfigurational ensemble starting from a single realization that has been first aged over 10^3 cycles. The distance matrix d_{AB}, calculated between replicas after 10 additional cycles, reveals a complex organization of states in the network model, whereas the hysteron model remains confined to the same few well-separated states.

To this end, we construct an isoconfigurational ensemble of simulations for each model (70). Namely, we run many simulations with the same initial condition, driving protocol, and temperature, but with different realizations of the thermal fluctuations. To quantify how different realizations diverge from each other and explore the space of possible states and limit cycles, we compute the interrealization distance $d_{AB} = \frac{1}{4N} \sum (\boldsymbol{s}_A - \boldsymbol{s}_B)^2$, where $\boldsymbol{s}_A$ and $\boldsymbol{s}_B$ are the binary states of two copies at a certain time.

We first compare the evolution of d_{AB} for two models during aging under static drive. For the coupled hysteron model, we find that the mean interrealization distance $\langle d_{AB}(t) \rangle$ increases, overshoots, and then saturates at a low value (Fig. 7 *A* and *Inset*). In contrast, for the network model $\langle d_{AB}(t) \rangle$ grows logarithmically throughout the evolution (Fig. 7 *B* and *Inset*). In other words, in the network model, copies of the same bistable network diverge from each other under different realizations of the noise. Copies of the same hysteron model follow essentially the same path of states, implying a much simpler organization. This is also visible in the full distribution of intercopy distances $P(d_{AB})$ (Fig. 7 *A* and *B*). Although this implies that the mechanism for aging is fundamentally different, both models exhibit similar logarithmic aging under static drive.

We now consider the two models under cyclic driving. The initial condition for the isoconfigurational ensemble is a limit cycle reached after a transient at $T = 0$ (*Materials and Methods*). We then switch on temperature, and follow d_{AB} stroboscopically as a function of the number of driving cycles n. While different realizations of the coupled hysteron model under cyclic driving do not diverge away from each other, and slowly converge to a fixed distribution $P(d_{AB})$ (Fig. 7*C*), we find that copies of the network model diverge logarithmically from each other and $P(d_{AB})$ becomes wider (Fig. 7*D*). To gain additional insight, we represent the set of d_{AB} after many driving cycles in the form of a matrix, where each element represents the distance between two particular copies (54). The results reveal that while the hysteron model explores only a small, discrete number of limit cycles (Fig. 7*E*), the network model exhibits a complex organization of the different copies (Fig. 7*F*), where each realization takes a distinct, separate path in its exploration of the energy landscape.

To further explore the structure of the energy landscape, we construct another ensemble of replicas, for which the initial condition is one of the well-aged realizations. Namely, we take a single realization from the previous ensemble, and use this well-aged system as the initial condition for a second isoconfigurational ensemble, which is run for an additional 10 cycles. This allows us to separate initial transients from the local exploration of the space of possible limit cycles at later stages. For the hysteron model, we again find only a few possible states, separated by large distances d_{AB} (Fig. 7*G*). In *SI Appendix*, we show that these states are precisely the ones explored by the first ensemble. For the network model, on the other hand, we find a multitude of states with rather small distances. We sort the different copies based on the distances d_{AB} using a hierarchical clustering algorithm (71). This reveals that the intercopy distance matrix has a hierarchical structure of states nested within each other (Fig. 7*H*).

Formally, the fact that different copies reach different regions of configuration space is a dynamical signature of replica symmetry breaking (RSB) (50–54). For the hysteron model, the peaked intercopy distance distribution (Fig. 7*C*) and the simple organization of the distance matrices (Fig. 7 *E* and *G*) is consistent with a 1-step RSB, associated to an energy landscape with relatively few, well-separated basins. In contrast, the continuous intercopy distance distribution observed in the

network model (Fig. 7*D*), together with the complex structure of the corresponding distance matrices (Fig. 7 *F* and *H*), exhibit characteristics of full RSB. This is indicative of a substantially more intricate landscape, where states are organized hierarchically. Indeed, disordered systems which show signatures of full RSB are known to exhibit complex aging effects (54). In contrast, 1-step RSB is often associated with the lack of aging (54, 72).

These results clearly discriminate between the two models. At long times, the noisy hysteron model becomes confined to a small part of configuration space, and the system converges to a multistable steady state, in which the response alternates between a small set of options. As a result, the transient slow decay of dissipation comes to a halt. In contrast, the bistable spring network continues to explore its configuration space, albeit at a slowing pace, without showing signs of approaching such a steady-state. This exploration allows the system to continuously find cycles with less and less dissipation.

One important caveat is that both models contain a substantial amount of parameters, and while we cannot rule out that there are parameter ranges or interaction types (60) where the hysteron model would become closer to the network model, at present we have no indications that this would be the case. Future work could investigate finite-size scaling in the thermal coupled hysterons model, or explore interaction structures beyond reciprocal and pairwise couplings.

Discussion

In this work, we have uncovered an aging phenomenon exhibited by different amorphous materials under long-term cyclic driving: a logarithmic decay of the dissipation per cycle. The results were used to discriminate between different models of amorphous matter. In particular, we compared two seemingly similar mesoscopic models: an ensemble of bistable degrees of freedom (hysterons) with reciprocal pairwise interactions, and a structural model of a disordered network of bistable elastic elements. While both capture aging under static strain, only the network model captures the full range of experimental results, including the observed aging under cyclic drive. This was shown to result from qualitatively different internal dynamics: only the network model exhibits the dynamical signatures of well-developed RSB. This suggests that cyclic aging arises when the energy landscape is composed of many competing attractors, allowing it to continuously explore phase space without getting trapped. While we believe that static aging originates from a similar mechanism (13), cyclic aging seems to be more discriminative, possibly due to the numerous intermediate states visited during each drive cycle.

What, then, are the crucial ingredients that enable the network model to more accurately capture the behavior of amorphous matter? We point to two key aspects. First is the continuous nature of the bistable degrees of freedom in the network model. As we have recently shown, the frustrated elastic interactions in such networks result in the self-organization of the system into a marginally stable state, in which the barrier for local activations becomes vanishingly small (14, 47). This persistent property of the network model replenishes the population of low energy barriers and facilitates exploration of the configuration space even at very low temperatures. This property seems to be missing in the coupled hysteron model, where small barriers are depleted over time and the structural evolution comes to a halt.

The second interesting difference is that the network model includes geometric effects which result in complex nonlinear and nonpairwise interactions between the bistable elements (65). This aspect, absent in the hysteron model studied here, may qualitatively change the complexity of the system's dynamics, and contribute to the slow exploration under cyclic drive.

Further work is needed in order to establish the necessity of these components for explaining the properties of amorphous media. Particularly, it would be interesting to explore whether thermal elastoplastic models (14, 73, 74), which are close relatives of our hysteron model (75, 76), exhibit aging under cyclic driving. Yet, our finding suggests a clear advantage for studying structural models with continuous degrees of freedom, rather than discrete ones.

Aging under cyclic driving can thus serve as a valuable protocol for probing complex behaviors using only global mechanical measurements (21). In particular, the universal logarithmic decay of dissipation per cycle may serve to probe whether the energy landscape of a disordered material is simple or hierarchical (53). On the other hand, the nonuniversal Material Creep Function provides a fingerprint for amorphous materials. These results may have practical implications for experiments in which amorphous matter is cyclically driven, from irreversibility transitions (77, 78) and memory formation (3, 57), to oscillatory yielding and fatigue, which are typically studied at larger amplitudes (25, 26, 30).

Finally, we stress that our approach combines key aspects of glassy physics: logarithmic aging and complex driving protocols usually used in the study of memory effects. As a wide range of memory effects can be unveiled by more complex driving protocols, i.e. nested driving cycles (3, 79, 80) or asymmetric driving cycles with time-ordered amplitudes (18, 23, 61, 81, 82), we suggest that studying the long-time response to such driving protocols in glassy systems at finite temperature may provide additional insight into their underlying self-organization. This may also provide even more stringent tests for models that aim to capture these phenomena.

Materials and Methods

Experimental.

Crumpled sheets. Thin sheets of Mylar, 50 cm by 50 cm across and 8 μm thick, are manually crumpled several times to form a disordered network of folds and creases. The sheets are then loosely formed to the shape of a ball and inserted to a custom mechanical tester described in ref. 49. The position of the stage U is driven with a precision of 50 μm, while the normal force F is measured. We note that the forces measured during driving are very small compared to the violent forces applied during the crumpling process. This ensures that the generation of new creases during our experiments is negligible (83).

In the static experiments, the system is abruptly compressed by $\Delta U = 10$ mm at a velocity $v = 5$ mm/s. In the cyclic experiments, the stage is driven along $U \in [0, 10]$ mm at a constant velocity $v = 1$ mm/s. Note that $U = 0$ is set arbitrarily at low force, but does not represent the free state where $F = 0$.

For acoustic measurements, we place the mechanical tester in a sound isolating chamber which reduces external noise by 10 dB and eliminates echoes (13). Inside the chamber a microphone records the acoustic emissions, whose waveforms have a typical frequency of 2 kHz. The acoustic signal is processed using a band pass filter, smoothed, and clicks are identified from peaks in the filtered signal. This allows distinguishing between separate events down to a resolution of 0.015 s.

Steel wool. Grade 000# steel wool, loosely shaped to a ball of diameter 10 cm, is inserted into the same custom mechanical tester. While the sample's edges are not clamped to the tester, we make sure it does not lose contact with the plates during driving.

For static experiments the system is compressed by $\Delta U = 20$ mm at a velocity $v = 5$ mm/s. For cyclic experiments the stage is driven along $U \in [80, 100]$ mm at a constant velocity $v = 1$ mm/s.

Nitinol wire. The shape memory wire is made of polycrystalline Nitinol (bought from Smart Wires©), with activation temperature $T_A \simeq 45\,^\circ$C and with diameter 1 mm . The shape of the Nitinol wire is set to be straight with a thermal annealing while constraining the wire's shape. This is done by repeating three times 12 min at 500 °C followed by an abrupt temperature quench in water. The Nitinol wires are then tested in torsion using a torsional INSTRON MT1-E1. A piece of straight wire of length L is placed into the collet of the testing machine, warmed up above its activation temperature with a heat gun for roughly 30 s, and cooled down for roughly 30 min. For static aging experiments, $L = 22$ mm, and the system is rotated by 360° at a constant speed $d\theta/dt = 90°/s$ before measuring the torque relaxation. For cyclic experiments, $L = 100$ mm, and the system is driven inside $\theta \in [0, \pi]$ at a constant speed $d\theta/dt = 10°/s$.

Coupled Hysterons Simulations.

Sampling. The midpoints (resp. the span) of the hysterons' hysteresis $\bar{u}_{i,0} = (u^+_{i,0} + u^-_{i,0})/2$ (resp. $\sigma_i = u^+_{i,0} - u^-_{i,0}$) are flatly sampled from $[-1, 1]$ (resp. from $[0.05, 0.5]$). The lower bound on the hysterons' spans allows preventing thermal fluctuations from snapping back and forth hysterons with a small span (see below). The interaction coefficients c_{ij} are also flatly sampled from $[-J_0, J_0]$, where J_0 is the typical interaction strength.

Simulation parameters. Noiseless simulations are used as a benchmark to measure the distribution of transient times τ and the ensemble averaged dissipation per cycle $\langle A_n \rangle$. In this case, unless stated otherwise, the driving amplitude $U_{\max}$ is chosen such that the magnetization of the hysteron model reaches $m = 0.5$ at $U_{\max}$ during the first driving cycle. For simulations including thermal fluctuations, the driving amplitude $U_{\max}$ is fixed without considering the system's magnetization. Moreover, the temperature T is chosen according to the following considerations. First, it must be small enough that thermal fluctuations remain negligible compared to the spans of the hysterons. The limit of small temperature is motivated by the network model, where it was shown that aging arises for any finite temperature (13, 14) (even when the thermal energy is far below the energy barrier between individual energy wells of a single spring $U(\delta R)$, see Fig. 5 *A*, *Inset*). Second, it should be sufficiently large to produce substantial logarithmic aging under static driving on accessible timescales. Third, for larger system sizes, we use smaller temperatures. Indeed, the key role of thermal fluctuations is to allow the system to escape a given limit-cycle response by reversing the flipping order of two hysterons within the driving cycle. Thus, the scale of thermal fluctuations relative to the typical distance between two instabilities (which itself depends on the number N of hysterons under the conventions adopted here) should remain fixed. Based on these considerations, we set $T = 10^{-4}$ for $N = 512$, and $T = 10^{-5}$ for $N = 2{,}048$.

Numerical integration. For noiseless cyclic drive simulations, we use an event-driven algorithm introduced in ref. 57 to simulate the sequence of hysteron flips as the input U is varied quasistatically. Similarly, for $T > 0$, we integrate the dynamics by moving forward in time instability-by-instability using the approach defined in ref. 74, further described below. Not only are event-driven methods very efficient computationally wise, but they also allow to make sure instabilities are systematically triggered one by one.

At a given time t, hysteron i has a distance to instability $\Delta U_i(t)$, and flips by thermal activation at rate $\lambda(\Delta U_i) = P(\xi_i > \Delta U_i)$ or immediately at $\Delta U_i = 0$. Working out the interevent period δt and site i is relatively trivial for fixed U, as activations happen at a given rate $\lambda(\Delta U_i)$. Since thermal activations are independent processes, with a waiting time probability distribution function $p(t) = \lambda(\Delta U_i) e^{-\lambda(\Delta U_i)t}$, for a system with N hysterons one could sample N random numbers $\{R_i \in [0, 1)\}$ and find the next activation time for each hysteron by inverting the cumulative distribution function for the waiting times, so that each hysteron is assigned a time $t_i = -\frac{1}{\lambda(\Delta U_i)} \ln(1 - R_i)$. By finding the hysteron with the smallest t_i, one has found the first hysteron to flip, and the appropriate interval $\delta t = t_i$. However, in cyclic drive simulations, the rates $\lambda(\Delta U_i(t))$ are not constant: $\Delta U_i(t) = \Delta U_i(t = 0) \pm vt$ (depending on the drive's direction and the state of hysteron i). In this case, for each hysteron we sample a random number $R_i \in [0, 1)$, and solve for t_i as

$$R_i = P(t < t_i) = \exp\left[-\int_0^{t_i} \lambda(\Delta U_i(t))dt\right]. \quad [4]$$

To solve Eq. **4** numerically, consider the related function $R(t) = \exp\left[-\int_0^t \lambda(\Delta U_i(t'))dt'\right]$, for which $R(t_i) = R_i$ is the desired solution. $R(t)$ obeys the following nonlinear ODE:

$$\frac{dR}{dt} = [1 - R(t)]\, \lambda(\Delta U_i(t)), \quad [5]$$

for which the initial value problem $R(t = 0) = 0$ and $R(t_i) = R_i$ (where R_i is still randomly drawn from $[0, 1)$) has a unique solution. We use SCIPY's solve-ivp routine (84) to integrate these equations for all hysterons simultaneously, halting when either $R(t_i) = R_i$ or $\Delta U_i = 0$ for any hysteron.

The system's preparation by stabilizing a random initial condition is performed at zero temperature. In static conditions, the quench by ΔU is simulated using the noiseless event-driven algorithm, so that the switching fields are considered fixed throughout the quench. However, from $t = 0$, the dynamics is computed using the stochastic event-driven simulation scheme. In cyclic drive conditions, the maximum drive amplitude $U_{\max}$ is determined during the first drive cycle by driving the system up to a magnetization $m = 0.5$, and keeping this maximum drive amplitude fixed for the rest of the simulation.

Bistable Spring Network Simulations.

Simulation details and parameters. We follow the simulation scheme detailed in ref. 13. Over-coordinated network topologies are obtained from jammed packings as detailed in ref. 49. We use large networks with $N = 2{,}000$ and $N = 10{,}000$ nodes ($N_b \approx 5{,}000$ and $N_b \approx 25{,}000$ bonds respectively). Each bond is assigned with random rest length $R_i^{(0)} \in [8, 11]$, and a potential given by Eq. **3** for deviations from the rest length $\delta R_i = R_i - R_i^{(0)}$. For all bonds the potential is identical with $\alpha_2 = 2.5$ and $\alpha_4 = 1$. These network parameters follow from previous works (13, 47) and were not optimized further. Yet we note that choosing different parameters or forms of the bistable potentials does not qualitatively change the behavior we report. In *SI Appendix*, we show that cyclic aging persists when the smooth potential of Eq. **3** is replaced by a cusped bistable potential.

We use the molecular dynamics platform LAMMPS (66). Brownian dynamics are simulated with a Langevin thermostat, an integration timestep $dt = 0.005$, a damping coefficient $\beta = 0.5$, and varying temperatures T. T is chosen to be very small compared to the potential barrier of a single bond $\Delta U_0 = \alpha_2^2/(4\alpha_4)$, consistently with previous work (13). At large enough T, noise is sufficient to spontaneously flip all bonds in the network, and the aging behavior is lost. Conversely, at low enough T aging is too minute to be observed for the system sizes at study (*SI Appendix*).

We use fixed boundary conditions. Cyclic biaxial strain is realized by setting a constant velocity v to the top and right boundaries of the network in the directions $\hat{y}$ and $\hat{x}$ respectively. The bottom and left boundaries are pinned in $\hat{y}$ and $\hat{x}$, respectively, and are free to move along the perpendicular axes. The cyclic strain amplitude $\gamma_{\max}$ is chosen such that at $T = 0$ the network reaches a limit cycle after several cycles (*SI Appendix*). At larger amplitudes, the network cannot reach a limit cycle even at $T = 0$, but instead exhibits a steady erratic evolution (85).

Network preparation. Before applying strain, we prepare each network at $T = 0$ and constant strain to reach a local mechanical equilibrium. The magnetization $m = \sum_i s_i/N_b$ at the beginning of cyclic driving, which we denote m_0, can be tuned by applying a constant force F_{prep} to the network's boundaries during preparation at $T = 0$. This also sets the initial system size L.

For static aging simulations, we apply an abrupt change in strain from zero to $\gamma_{\max} = 4.5\%$ at a velocity $v = 2$ and $T = 0$, before turning on $T > 0$.

Isoconfigurational Ensemble. The isoconfigurational ensemble is prepared by creating a single realization of disorder (either for hysterons or the network

model) as described above, and by cyclically driving this realization at $T = 0$ until reaching a limit cycle. From this point, we simulate multiple copies of the system, each with a different realization of thermal fluctuations, for $n = 1{,}000$ cycles.

In a second step, we choose a single realization that has evolved over 1,000 cycles as the initial condition for the isoconfigurational ensemble. Namely, we simulate copies of this well-aged system to follow how they locally explore the energy landscape.

Number of Instabilities. For both the hysteron model and the network model, we define the number of instabilities over the n-th driving cycle $N_i(n)$ as the sum of the numbers of elements which have flipped during the increasing and decreasing phases. These are determined by comparing the system's configurations (the binarized state for the network model) at the lowest and largest values of the drive.

Data, Materials, and Software Availability. Data and codes have been deposited in Zenodo (TBD) (86).

ACKNOWLEDGMENTS. We thank Oren Raz for fruitful discussions and Olivier Dauchot for helpful comments. This work was supported by the Israel Science Foundation grant 2117/22. P.B. and M.v.H. acknowledge funding from European Research Council Grant ERC-101019474. D.S. acknowledges support from the Clore Israel Foundation.

Author affiliations: [a]Department of Condensed Matter Physics, School of Physics and Astronomy, Tel Aviv University, Tel Aviv 69978, Israel; [b]The Center for Physics and Chemistry of Living Systems, Tel Aviv University, Tel Aviv 69978, Israel; [c]Information in Matter, AMOLF, Amsterdam 1098 XG, The Netherlands; [d]Sino-Europe Complexity Science Center, School of Mathematics, North University of China, Shanxi, Taiyuan 030051, China; [e]Department of Chemical and Biological Physics, Faculty of Chemistry, The Weizmann Institute of Science, Rehovot 76100, Israel; and [f]Huygens-Kamerlingh Onnes Laboratory, Leiden University, Leiden 2300 RA, The Netherlands

1. J. P. Sethna, K. A. Dahmen, C. R. Myers, Crackling noise. *Nature* **410**, 242–250 (2001).
2. F. Arceri, F. P. Landes, L. Berthier, G. Biroli, "A statistical mechanics perspective on glasses and aging" in *Encyclopedia of complexity and systems science*, R. A. Meyers, Ed. (Springer, Berlin, Heidelberg, 2021), pp. 1–68.
3. N. C. Keim, J. D. Paulsen, Z. Zeravcic, S. Sastry, S. R. Nagel, Memory formation in matter. *Rev. Mod. Phys.* **91**, 035002 (2019).
4. D. Tapias, C. Marteau, F. Aguirre-López, P. Sollich, Bringing together two paradigms of nonequilibrium: Fragile versus robust aging in driven glassy systems. *Phys. Rev. Lett.* **133**, 197101 (2024).
5. A. Kovacs, Glass transition in amorphous polymers: A phenomenological study. *Adv. Polym. Sci.* **3**, 394–507 (1963).
6. J. B. Knight, C. G. Fandrich, C. N. Lau, H. M. Jaeger, S. R. Nagel, Density relaxation in a vibrated granular material. *Phys. Rev. E* **51**, 3957 (1995).
7. O. Ben-David, S. M. Rubinstein, J. Fineberg, Slip-stick and the evolution of frictional strength. *Nature* **463**, 76–79 (2010).
8. D. M. Kaz, R. McGorty, M. Mani, M. P. Brenner, V. N. Manoharan, Physical ageing of the contact line on colloidal particles at liquid interfaces. *Nat. Mater.* **11**, 138–142 (2012).
9. K. Matan, R. B. Williams, T. A. Witten, S. R. Nagel, Crumpling a thin sheet. *Phys. Rev. Lett.* **88**, 076101 (2002).
10. Y. Lahini, O. Gottesman, A. Amir, S. M. Rubinstein, Nonmonotonic aging and memory retention in disordered mechanical systems. *Phys. Rev. Lett.* **118**, 085501 (2017).
11. J. P. Bouchaud, Weak ergodicity breaking and aging in disordered systems. *J. Phys.* **I**, 1705–1713 (1992).
12. D. M. Robe, S. Boettcher, P. Sibani, P. Yunker, Record dynamics: Direct experimental evidence from jammed colloids. *Europhys. Lett.* **116**, 38003 (2016).
13. D. Shohat, Y. Friedman, Y. Lahini, Logarithmic aging via instability cascades in disordered systems. *Nat. Phys.* **19**, 1890–1895 (2023).
14. D. J. Korchinski, D. Shohat, Y. Lahini, M. Wyart, Thermal avalanches drive logarithmic creep in disordered media. *Phys. Rev. X* **15**, 031024 (2025).
15. L. Corte, P. M. Chaikin, J. P. Gollub, D. J. Pine, Random organization in periodically driven systems. *Nat. Phys.* **4**, 420–424 (2008).
16. I. Regev, T. Lookman, C. Reichhardt, Onset of irreversibility and chaos in amorphous solids under periodic shear. *Phys. Rev. E* **88**, 062401 (2013).
17. J. D. Paulsen, N. C. Keim, Mechanical memories in solids, from disorder to design. *Annu. Rev. Condens. Matter Phys.* **16**, 61–81 (2024).
18. J. D. Paulsen, N. C. Keim, S. R. Nagel, Multiple transient memories in experiments on sheared non-Brownian suspensions. *Phys. Rev. Lett.* **113**, 068301 (2014).
19. D. Fiocco, G. Foffi, S. Sastry, Encoding of memory in sheared amorphous solids. *Phys. Rev. Lett.* **112**, 025702 (2014).
20. M. Mungan, S. Sastry, K. Dahmen, I. Regev, Networks and hierarchies: How amorphous materials learn to remember. *Phys. Rev. Lett.* **123**, 178002 (2019).
21. D. Shohat, Y. Lahini, Dissipation indicates memory formation in driven disordered systems. *Phys. Rev. Lett.* **130**, 048202 (2023).
22. H. Bense, M. van Hecke, Complex pathways and memory in compressed corrugated sheets. *Proc. Natl. Acad. Sci. U.S.A.* **118**, e2111436118 (2021).
23. J. Liu *et al.*, Controlled pathways and sequential information processing in serially coupled mechanical hysterons. *Proc. Natl. Acad. Sci. U.S.A.* **121**, e2308414121 (2024).
24. L. J. Kwakernaak, M. van Hecke, Counting and sequential information processing in mechanical metamaterials. *Phys. Rev. Lett.* **130**, 268204 (2023).
25. P. Das, H. Vinutha, S. Sastry, Unified phase diagram of reversible-irreversible, jamming, and yielding transitions in cyclically sheared soft-sphere packings. *Proc. Natl. Acad. Sci. U.S.A.* **117**, 10203–10209 (2020).
26. H. Bhaumik, G. Foffi, S. Sastry, The role of annealing in determining the yielding behavior of glasses under cyclic shear deformation. *Proc. Natl. Acad. Sci. U.S.A.* **118**, e2100227118 (2021).
27. D. Fiocco, G. Foffi, S. Sastry, Oscillatory athermal quasistatic deformation of a model glass. *Phys. Rev. E* **88**, 020301 (2013).
28. Y. Zhao *et al.*, Ultrastable shear-jammed granular material. *Phys. Rev. X* **12**, 031021 (2022).
29. J. T. Parley, S. Sastry, P. Sollich, Mean-field theory of yielding under oscillatory shear. *Phys. Rev. Lett.* **128**, 198001 (2022).
30. S. Maity, H. Bhaumik, S. Athani, S. Sastry, Fatigue failure in glasses under cyclic shear deformation. arXiv [Preprint] (2024). http://arxiv.org/abs/2409.17384 (Accessed 19 January 2026).
31. J. O. Cochran, G. L. Callaghan, M. J. Caven, S. M. Fielding, Slow fatigue and highly delayed yielding via shear banding in oscillatory shear. *Phys. Rev. Lett.* **132**, 168202 (2024).
32. N. V. Priezjev, Heterogeneous relaxation dynamics in amorphous materials under cyclic loading. *Phys. Rev. E* **87**, 052302 (2013).
33. P. K. Jana, N. V. Priezjev, Relaxation dynamics in amorphous alloys under asymmetric cyclic shear deformation. *J. Non-Cryst. Solids* **600**, 121996 (2023).
34. D. Majumdar, I. Regev, Memory switching due to thermal noise in amorphous solids subject to cyclic shear. arXiv [Preprint] (2023). http://arxiv.org/abs/2310.09869 (Accessed 19 January 2026).
35. P. Das, A. D. Parmar, S. Sastry, Annealing glasses by cyclic shear deformation. *J. Chem. Phys.* **157**, 044501 (2022).
36. N. V. Priezjev, Structural relaxation and delayed yielding in cyclically sheared Cu-Zr metallic glasses. *Metals* **14**, 984 (2024).
37. N. V. Priezjev, Mechanical annealing and yielding transition in cyclically sheared binary glasses. *J. Non-Cryst. Solids* **590**, 121697 (2022).
38. M. Bandi, H. G. E. Hentschel, I. Procaccia, S. Roy, J. Zylberg, Training, memory and universal scaling in amorphous frictional granular matter. *Europhys. Lett.* **122**, 38003 (2018).
39. S. M. Fielding, P. Sollich, M. E. Cates, Aging and rheology in soft materials. *J. Rheol.* **44**, 323–369 (2000).
40. A. Shukla, S. Shanbhag, Y. M. Joshi, Analysis of linear viscoelasticity of aging soft glasses. *J. Rheol.* **64**, 1197–1207 (2020).
41. J. R. Macdonald, Linear relaxation: Distributions, thermal activation, structure, and ambiguity. *J. Appl. Phys.* **62**, R51–R62 (1987).
42. R. V. Chamberlin, Experiments and theory of the nonexponential relaxation in liquids, glasses, polymers and crystals. *Phase Trans. A Multinatl. Journal* **65**, 169–209 (1998).
43. A. Amir, S. Borini, Y. Oreg, Y. Imry, Huge (but finite) time scales in slow relaxations: Beyond simple aging. *Phys. Rev. Lett.* **107**, 186407 (2011).
44. A. Amir, Y. Oreg, Y. Imry, On relaxations and aging of various glasses. *Proc. Natl. Acad. Sci. U.S.A.* **109**, 1850–1855 (2012).
45. F. Preisach, Über die magnetische nachwirkung. *Z. Phys.* **94**, 277–302 (1935).
46. M. van Hecke, Profusion of transition pathways for interacting hysterons. *Phys. Rev. E* **104**, 054608 (2021).
47. D. Shohat, Y. Lahini, D. Hexner, Emergent marginality in frustrated multistable networks. *J. Chem. Phys.* **162**, 114505 (2025).
48. L. Yan, G. Düring, M. Wyart, Why glass elasticity affects the thermodynamics and fragility of supercooled liquids. *Proc. Natl. Acad. Sci. U.S.A.* **110**, 6307–6312 (2013).
49. D. Shohat, D. Hexner, Y. Lahini, Memory from coupled instabilities in unfolded crumpled sheets. *Proc. Natl. Acad. Sci. U.S.A.* **119**, e2200028119 (2022).
50. G. Parisi, Order parameter for spin-glasses. *Phys. Rev. Lett.* **50**, 1946 (1983).
51. M. Mézard, G. Parisi, N. Sourlas, G. Toulouse, M. Virasoro, Replica symmetry breaking and the nature of the spin glass phase. *J. Phys.* **45**, 843–854 (1984).
52. M. Mézard, G. Parisi, M. A. Virasoro, *Spin Glass Theory and Beyond: An Introduction to the Replica Method and Its Applications* (World Scientific Publishing Company, 1987), vol. 9.
53. P. Charbonneau, J. Kurchan, G. Parisi, P. Urbani, F. Zamponi, Fractal free energy landscapes in structural glasses. *Nat. Commun.* **5**, 3725 (2014).
54. C. Scalliet, L. Berthier, F. Zamponi, Nature of excitations and defects in structural glasses. *Nat. Commun.* **10**, 5102 (2019).
55. Y. Lahini, S. M. Rubinstein, A. Amir, Crackling noise during slow relaxations in crumpled sheets. *Phys. Rev. Lett.* **130**, 258201 (2023).
56. N. C. Keim, J. Hass, B. Kroger, D. Wieker, Global memory from local hysteresis in an amorphous solid. *Phys. Rev. Res.* **2**, 012004 (2020).
57. N. C. Keim, J. D. Paulsen, Multiperiodic orbits from interacting soft spots in cyclically sheared amorphous solids. *Sci. Adv.* **7**, eabg7685 (2021).
58. N. C. Keim, D. Medina, Mechanical annealing and memories in a disordered solid. *Sci. Adv.* **8**, eabo1614 (2022).
59. C. W. Lindeman, T. R. Jalowiec, N. C. Keim, Generalizing multiple memories from a single drive: The hysteron latch. *Sci. Adv.* **11**, eadr5933 (2025).
60. P. Baconnier, M. H. Teunisse, M. van Hecke, Dynamic self-loops in networks of passive and active binary elements. *Phys. Rev. Lett.* **135**, 207402 (2025).
61. C. W. Lindeman, T. R. Jalowiec, N. C. Keim, Generalizing multiple memories from a single drive: The hysteron latch. *Sci. Adv.* **11**, eadr5933 (2025).
62. J. J. Hopfield, Neural networks and physical systems with emergent collective computational abilities. *Proc. Natl. Acad. Sci. U.S.A.* **79**, 2554–2558 (1982).
63. C. W. Lindeman, S. R. Nagel, Multiple memory formation in glassy landscapes. *Sci. Adv.* **7**, eabg7133 (2021).
64. C. W. Lindeman, S. R. Nagel, Minimal cyclic behavior in sheared amorphous solids. *New J. Phys.* **27**, 085001 (2025).

65. D. Shohat, M. van Hecke, Geometric control and memory in networks of hysteretic elements. *Phys. Rev. Lett.* **134**, 188201 (2025).
66. A. P. Thompson *et al*., Lammps-a flexible simulation tool for particle-based materials modeling at the atomic, MESO, and continuum scales. *Comput. Phys. Commun.* **271**, 108171 (2022).
67. I. Procaccia, T. Samanta, Energy dissipation in cyclic strain of amorphous solids. arXiv [Preprint] (2025). http://arxiv.org/abs/2505.13035 (Accessed 19 January 2026).
68. E. M. Kramer, A. E. Lobkovsky, Universal power law in the noise from a crumpled elastic sheet. *Phys. Rev. E* **53**, 1465 (1996).
69. P. A. Houle, J. P. Sethna, Acoustic emission from crumpling paper. *Phys. Rev. E Stat. Phys. Plasmas Fluids Relat. Interdiscip. Topics* **54**, 278–283 (1996).
70. A. Widmer-Cooper, P. Harrowell, H. Fynewever, How reproducible are dynamic heterogeneities in a supercooled liquid? *Phys. Rev. Lett.* **93**, 135701 (2004).
71. F. Murtagh, P. Contreras, Algorithms for hierarchical clustering: An overview. *Wiley Interdiscip. Rev. Data Min. Knowl. Discov.* **2**, 86–97 (2012).
72. C. Scalliet, L. Berthier, F. Zamponi, Absence of marginal stability in a structural glass. *Phys. Rev. Lett.* **119**, 205501 (2017).
73. A. Nicolas, E. E. Ferrero, K. Martens, J. L. Barrat, Deformation and flow of amorphous solids: Insights from elastoplastic models. *Rev. Mod. Phys.* **90**, 045006 (2018).
74. D. Korchinski, J. Rottler, Dynamic phase diagram of plastically deformed amorphous solids at finite temperature. *Phys. Rev. E* **106**, 034103 (2022).
75. D. Kumar *et al*., Mapping out the glassy landscape of a mesoscopic elastoplastic model. *J. Chem. Phys.* **157**, 174504 (2022).
76. D. Kumar, M. Mungan, S. Patinet, M. M. Terzi, D. Vandembroucq, Self-organization and emergence of memory in a cyclically driven elastoplastic model of an amorphous solid. *Phys. Rev. E* **112**, 035411 (2025).
77. I. Regev, T. Lookman, "The irreversibility transition in amorphous solids under periodic shear" in *Avalanches in Functional Materials and Geophysics*, E. K. H. Salje, A. Saxena, A. Planes, Eds. (Springer International Publishing, 2017), pp. 227–259.
78. C. Reichhardt, I. Regev, K. Dahmen, S. Okuma, C. J. O. Reichhardt, Reversible to irreversible transitions in periodic driven many-body systems and future directions for classical and quantum systems. *Phys. Rev. Res.* **5**, 021001 (2023).
79. J. P. Sethna *et al*., Hysteresis and hierarchies: Dynamics of disorder-driven first-order phase transformations. *Phys. Rev. Lett.* **70**, 3347 (1993).
80. O. Perković, J. P. Sethna, Improved magnetic information storage using return-point memory. *J. Appl. Phys.* **81**, 1590–1597 (1997).
81. S. Coppersmith *et al*., Self-organized short-term memories. *Phys. Rev. Lett.* **78**, 3983 (1997).
82. N. C. Keim, S. R. Nagel, Generic transient memory formation in disordered systems with noise. *Phys. Rev. Lett.* **107**, 010603 (2011).
83. J. Andrejevic, L. M. Lee, S. M. Rubinstein, C. H. Rycroft, A model for the fragmentation kinetics of crumpled thin sheets. *Nat. Commun.* **12**, 1470 (2021).
84. P. Virtanen *et al*., Scipy 1.0: Fundamental algorithms for scientific computing in python. *Nat. Methods* **17**, 261–272 (2020).
85. S. Huang, D. Hexner, Banding and polarization in driven multistable materials. *J. Chem. Phys*. **163**, 214504 (2025).
86. D. Shohat *et al*., Aging of amorphous materials under cyclic strain. Zenodo. https://zenodo.org/records/18314148. Deposited 19 January 2026.